Trapping Devices of Carnivorous fungus *Arthrobotrys oligospora* is a Phenotypic System for Separating Thermally-Induced Excess Irons

Jiao Zhou,[⊥] Qunfu Wu,[⊥] Li Wu, Junxian Yan, Qianyi Cheng, Donglou Wang, Xuemei Niu*

State Key Laboratory for Conservation and Utilization of Bio-Resources in Yunnan, School of Life Sciences, Key Laboratory for Microbial Resources of the Ministry of Education, Yunnan University, Kunming 650091, P. R. China.

[⊥]These authors contributed equally to this paper

*To whom correspondence should be addressed. Tel: 86-871-65032538; Fax: 86-871-65034838. E-mail: xmniu@ynu.edu.cn (Xuemei Niu).

Abstract

The discovery of eukaryotes with an iron overload phenotype offers promising insights for developing treatments and strategies for human iron overload diseases caused by genetic defects. Under nutrient-limited conditions, *Arthrobotrys oligospora* and other nematode-trapping fungi (NTF) can differentiate their mycelia into specialized structures to capture prey as a nutritional source. Recent work has shown that siderophore deficiency worsens the discrepancies between trapping device development and fungal carnivorous activity in *A. oligospora*, previously believed to indicate a degeneration of its carnivorous capacity. Using transmission electron microscopy, energy-dispersive X-ray spectroscopy, and functional analyses, we identified siderophore-deficient mutants that develop numerous trapping devices but lack a significant number of iron-containing ferrichrome granules and exhibit autophagosomes in their mycelia. Notably, the electron-dense bodies in trapping devices store more iron than vacuoles and mitochondria. Genomic analysis revealed that NTFs lack the crucial CccA-mediated vacuolar iron detoxification pathway, which is conserved in most fungi. Bayesian relaxed molecular clock analysis suggested that the evolution of NTFs coincided with global warming. We demonstrated that the trapping devices of *A. oligospora*, triggered by high temperatures, function as a system to sequester excess iron, thus preventing abnormal free iron levels in mycelia and aiding the fungi in adapting to hot environments. Our findings identify a non-trophic environmental factor that triggers iron overload and a phenotypic indicator of iron overload in eukaryotes. This suggests that NTFs could serve as a potential eukaryotic model for elucidating the dynamic regulation mechanisms of iron homeostasis, potentially aiding in the treatment of iron overload-induced diseases in humans.

Author summary

Iron overload, whether caused by genetic or acquired factors, can lead to iron poisoning, hemochromatosis, and a range of serious diseases. Caucasians are particularly susceptible to iron overload and the complications of hemochromatosis due to a higher incidence of mutations in the homeostatic iron regulation gene within this population. The discovery of eukaryotes exhibiting an iron overload phenotype has significant implications for developing treatments and strategies for human iron overload diseases linked to genetic defects.

We discovered that a unique group of carnivorous fungi has evolved to develop trapping devices to sequester excess iron due to the absence of the crucial CccA-mediated vacuolar iron detoxification mechanism, which is conserved in most fungi. Furthermore, we report for the first time that high temperature is a non-trophic factor that induces iron overload in eukaryotes, as iron content and composition in fungal mycelia are negatively correlated with temperature. Our findings suggest that nematode-trapping fungi could serve as a potential eukaryotic model for elucidating the dynamic regulation mechanisms of iron homeostasis, which could contribute to treating iron overload-induced diseases in humans.

Key words: Nematode-trapping fungi, iron sequestration, phenotypic system, *Arthrobotrys oligospora*

Introduction

The ability to segregate excess elements in response to environmental changes is vital for survival and fitness in all organisms. Iron overload leads to cellular toxicity due to the generation of oxyradicals and lipid membrane peroxidation [1]. In eukaryotes, a key method of iron storage is through ferritin or siderophore-mediated sequestration [2–4]. Ferritins serve as the primary iron storage system in animals, plants, and most microbes [5–7]. In fungi, siderophores are widely distributed and function as iron storage compounds by forming ferri-siderophore complexes. Additionally, in pathogenic fungi, siderophores are often suggested to act as virulence factors, making siderophore biosynthesis a potential target for antifungal chemotherapy against *Candida albicans*, as the underlying biochemical pathways are absent in human cells. Desferriferrichrome, the first known siderophore, was isolated from the corn smut fungus *Ustilago sphaerogena* in 1952 and is widely distributed in fungi as a well-known siderophore for iron uptake and storage [8,9]. The biosynthesis of desferriferrichrome, derived from L-ornithine and glycine, involves a L-ornithine N(5)-oxygenase (LOO) and a nonribosomal peptide synthetase (NRPS).

Recent work has reported that a predominant nematode-trapping fungus (NTF) *Arthrobotrys oligospora* also produces desferriferrichrome via two genes *Ao414* and *Ao415*, which encode a LOO and a NRPS, respectively [8]. NTFs are a heterogeneous group of carnivorous fungi belonging to the Orbiliomycetes class within Ascomycota phylum. These fungi are known for their ability to sense environmental changes, such as the presence of nematodes, under nutrient deprivation and trigger the development of sophisticated nematode-trapping devices, enabling them to exploit nematodes, other small animals, and protozoans as their nutrient sources [10, 11]. NTFs form a monophyletic group with various trapping devices, including adhesive columns (AC), adhesive knobs (AK), adhesive networks (AN), and constricting rings (CR) [12,13]. Importantly, NTFs are among the most effective agents for controlling nematode populations and have been extensively studied for their potential as biological control agents for pathogenic nematodes [14]. While the development and behavior of trapping devices have been well-documented, growing evidence suggests that the degeneration of carnivorous ability characterizes the evolution of NTFs [12].

Recent studies have shown that deficiencies in *Ao414* or *Ao415* not only cause *A. oligospora* to lose desferriferrichrome but also trigger the mass production of trapping devices from mycelia in the mutants Δ*Ao414* and Δ*Ao415*, compared to the wild type (WT) [8]. Furthermore, the Δ*Ao414* mutant, which lacks any desferriferrichrome precursors, develops significantly more trapping devices than the Δ*Ao415* mutant, which retains the desferriferrichrome precursor that can still sequester iron [8]. However, both Δ*Ao414* and Δ*Ao415* mutants exhibit reduced carnivorous ability. Additionally, iron supplementation enhances the development of trapping devices in *A. oligospora* but impairs the fungus's carnivorous ability. The mechanisms behind the iron sequestration in inhibiting the development of trapping devices warrant further investigation.

Fungal mycelia exhibit decision-making abilities, altering their developmental patterns in response to environmental changes by adjusting metabolic and cellular processes [15]. Mycelia can be microscopic or develop into visible structures such as brackets, mushrooms, puffballs, rhizomorphs (long strands of hyphae cemented

together), sclerotia (hard, compact masses), stinkhorns, toadstools, and truffles. At a certain stage, mycelia produce spores, either directly or through specialized fruiting bodies [16]. The trapping devices of nematode-trapping fungi (NTFs) develop from vegetative mycelia. However, the cellular changes and chemical properties in the mycelia that differentiate into trapping devices remain largely unknown. That is, what is the key difference in mycelium cells between two mutants Δ*Ao414* and Δ*Ao415*, and WT, which causes the mutant strain to form a large number of trapping devices.

As a starting point, we investigated the cellular changes occurring in *A. oligospora* mycelia in response to the absence of siderophores. Previous studies established that a large mass of electron-dense bodies is a diagnostic indicator for trapping devices [17, 18], yet the chemical properties of these bodies remained unclear. To elucidate these properties, we employed energy-dispersive X-ray spectroscopy in conjunction with transmission electron microscopy (TEM). Our findings revealed that the mycelia with the absence of siderophores lost a substantial amount of iron-containing ferrichrome granules, while electron-dense bodies within trapping devices stored significantly more iron than vacuoles and mitochondria. The inadequacy of less potent vacuoles for iron storage led us to discover that NTFs lack five key iron-related orthologous genes, including the essential vacuolar iron transporter *CccA* gene, which is widely distributed and highly conserved across fungi. A Bayesian relaxed molecular clock analysis, utilizing 275,133 four-fold degenerate sites from 1,136 single-copy orthologous genes and three fossil calibration points, indicated that both the acquisition of siderophore biosynthesis and the divergence of fungal carnivorism from saprophytism coincided with global warming. Functional analyses demonstrated that a reduction in temperature strongly inhibited the development of trapping devices, even with iron supplementation. Collectively, our work shows that NTFs develop trapping devices to sequester excess iron from mycelia and prevent iron overload at high temperatures due to a deficiency in vacuole-mediated iron storage. This adaptation is analogous to human thermoregulation: storing winter clothes when summer arrives and removing layers when temperatures rise. NTFs offer a promising eukaryotic model for evaluating and developing treatments and strategies for iron overload-induced diseases in humans.

Results

Desferriferrichrome for normal ferrichrome granules formation in mycelia

To better characterize the cellular changes that differentiate mycelia into trapping devices, we compared the structures of mycelial cells between WT and the two mutants, Δ*Ao414* and Δ*Ao415*. TEM analysis revealed that Δ*Ao414* lost most iron-containing ferrichrome granules in the mycelial cells compared to WT (Fig. 1a). In contrast, Δ*Ao415* exhibited aggregated large iron-containing granules distinct from those in WT (Fig. 1a). Notably, perophagy-like autophagosomes were present in some cells of both Δ*Ao414* and Δ*Ao415* mycelia but were absent in WT cells (Fig. 1a). The production of autophagosomes commonly associate with nutrient deficiency or hyphal senescence, suggesting that the absence of desferriferrichrome could exacerbates hyphal senescence or nutrient deficiency in mycelia. Furthermore, treatment with desferriferrichrome restored normal ferrichrome granule formation in the mycelia of

both mutants and increased ferrichrome granule formation in the mycelia of WT (Fig. 1b).

Desferriferrichrome-mediated ferrichrome granules effectively for iron storage in mycelia

Energy-dispersive X-ray spectroscopy (EDX) is a widely used technique for analyzing the elemental composition and distribution in nanomaterials [19]. In this study, the EDX detector was integrated into a transmission electron microscope (TEM) system to identify and quantify iron levels in ferrichrome granules within the fungal mycelial cells of both WT and the mutant Δ*Ao414*. Additionally, other organelles in these cells, including autophagosomes, vacuoles, mitochondria, and cell walls, were evaluated and compared with the ferrichrome granules. To better characterize the ferrichrome granules induced by desferriferrichrome, both WT and Δ*Ao414* were treated with and without desferriferrichrome.

We observed a significant Fe signal in the X-ray spectra from ferrichrome granules and mitochondria in both WT and the Δ*Ao414* mutant, regardless of whether they were treated with desferriferrichrome or not. This indicates that ferrichrome granules, like mitochondria, are involved in iron storage (Figs. 2a and S2). Interestingly, in Δ*Ao414* treated with desferriferrichrome, the EDX spectra showed an absence of Fe signal from autophagosomes and vacuoles, in stark contrast to the notable Fe signal observed from autophagosomes in Δ*Ao414* treated with only solvent (Figs. 2b and S2). This distinct difference suggests that *A. oligospora* preferentially utilizes desferriferrichrome for iron storage rather than relying on vacuoles or autophagosomes. Comparison of relative iron levels in ferrichrome granules and other organelles within the same mycelial cells of both WT and Δ*Ao414* revealed that desferriferrichrome-mediated ferrichrome granules contain more iron than mitochondria and autophagosomes (Figs. 2c and S2). These results indicate that desferriferrichrome plays a crucial role in iron storage within the mycelia.

Electron dense bodies in trapping devices mainly for iron storage and isolation

Trapping devices are characterized by the accumulation of numerous electron-dense bodies, whose components and physiological functions remain largely unknown. In WT, nematode-induced trapping devices exhibit a tendency for these electron-dense bodies to concentrate in one of the two separated cells, a phenomenon not observed in the mutants Δ*Ao414* and Δ*Ao415* (Fig. 3a). This observation suggests that desferriferrichrome regulates the aggregation and isolation of electron-dense bodies within trapping devices. Furthermore, iron supplementation resulted in a uniform morphology and size of the electron-dense bodies across all three strains—WT and the two mutants Δ*Ao414* and Δ*Ao415* (Fig. 3b).

A significant Fe signal was observed in the EDX spectra from the electron-dense bodies in the nematode-induced trapping devices of WT (Figs. 3c-d). Importantly, the iron levels in these electron-dense bodies were substantially higher than those in mitochondria and vacuoles within the same cells (Figs. 3d-e and S3). To compare iron levels between electron-dense bodies and desferriferrichrome-mediated ferrichrome granules, we analyzed cells containing both organelles in adequate quantities and proper distribution. However, desferriferrichrome-mediated ferrichrome granules

were primarily found in WT mycelia. We identified that cells from trapping devices of WT under iron treatment met these criteria effectively. Notably, desferriferrichrome-mediated ferrichrome granules exhibited significantly higher iron levels than the electron-dense bodies in the same cells (Figs. 4a–d and S4). Additionally, desferriferrichrome-mediated ferrichrome granules were much smaller than the electron-dense bodies (Fig. 4e). These results suggest that while electron-dense bodies serve as an alternative system for iron storage and isolation, they are less efficient compared to desferriferrichrome-mediated ferrichrome granules but more efficient than mitochondria and vacuoles.

To further assess the role of trapping devices in iron storage and isolation, we compared the iron levels in the mycelia and trapping devices of WT and the mutant Δ*Ao414*. Collecting sufficient amounts of trapping devices and mycelia from a single plate to meet measurement requirements was challenging. Moreover, the collected trapping devices often included a significant number of mycelia. Despite these difficulties, the combined samples of trapping devices and mycelia from both strains exhibited significantly higher levels of ferrous, ferric, and total iron compared to samples containing only mycelia (Figs. 4f-g). Notably, the ferric iron levels in the combined samples were 1.3-fold higher than those in the mycelia-only samples. Additionally, the combined samples showed a markedly reduced ratio of ferrous to ferric iron compared to the mycelia-only samples (Fig. 4f, g).

Absence of key iron-related genes in NTFs

To explore the genetic mechanisms underlying the differentiation of mycelia into trapping devices for iron storage, we analyzed the distribution and abundance of the 54 genes involved in iron sequestration and transport in NTFs. Our analysis revealed that all NTFs lack five specific orthologous genes: noranthrone synthase, siderophore biosynthesis acetylase, ferric-chelate reductase, metalloreductase, and the vacuolar iron transporter CccA (Fig. 5b and S2 Table). CccA is highly conserved across the fungal kingdom and is essential for importing iron into the vacuole to prevent toxic iron overload in the cytosol [20–22]. The observed dysfunction of vacuoles in iron storage in *A. oligospora*, supports the data that NTFs lack CccA-mediated vacuolar iron storage.

Further analysis of ferritin, a ubiquitous iron storage protein found in both prokaryotes and eukaryotes [23–25], revealed variability in its copy numbers among NTFs, depending on the type of trapping devices they possess. Specifically, one copy is present in species with adhesive networks (*Arthrobotrys oligospora* and *Arthrobotrys flagrans*), two copies in species with constricting rings (*Drechslerella brochopaga* and *Drechslerella dactyloides*), three copies in species with adhesive columns (*Dactylellina cionopaga*), and four copies in species with adhesive knobs (*Dactylellina haptotyla* and *Dactylellina entomopaga*) (Fig. 5b). Notably, the transcriptional level of ferritin in *A. oligospora* is very low (average TPM = 4.19) and remains unaffected by the inactivation of *Ao414* (S7 Fig). This suggests that the number and size of ferritin gene copies involved in iron sequestration and transport may contribute to the observed differences among NTFs.

Moreover, NTFs lack the ability to harbor ferrosomes, a class of iron storage

organelles encoded by the fezABC operon found in various bacteria and archaea, such as *Desulfovibrio magneticus*. This deficiency is attributed to the presence of only the homologous gene *FezB* [26,27], which encodes a P1B-6-ATPase, in NTFs. It is reasonable to assume that NTFs within the Orbiliomycetes class have developed alternative strategies to manage potential iron overload in their mycelia.

The evolutions of NTF coinciding with global high temperatures

Given the primary roles of ferrichrome and trapping devices in iron storage and isolation in *A. oligospora*, we investigated whether the origin of the *Ao415* gene cluster and the evolution of NTFs might be related to iron exposure. To elucidate the evolutionary trajectory of the *Ao415* cluster within the fungal kingdom, we conducted a comprehensive survey of gene clusters analogous to *Ao414* and *Ao415* across 1,488 high-quality fungal genomes (1,177 Ascomycota; 289 Basidiomycota; 21 Mucoromycota; 1 Zoopagomycota). We found that 744 fungal genomes contained homologs of the *Ao415* cluster, all of which were from Ascomycetes (Fig. 5a and S3 Table). A time-calibrated phylogenetic tree is needed to further understand this evolution. However, the evolutionary origin of carnivorous fungi remains debated, with conflicting estimates of divergence times for fungal carnivorism in Orbiliomycetes (Ascomycota). This uncertainty may be attributed to: 1) inaccuracies in fossil calibrations, as the earliest known fossil of carnivorous fungi, *Palaeoanellus dimorphus*, dates to the early Cretaceous, approximately 100 million years ago [29]; 2) the limited number of genes analyzed [12,13]; and 3) high variations in evolutionary rates among fungal lineages [30]. These issues could potentially be addressed by employing more precise rate estimation methods that utilize an adequate number of genes and focus exclusively on four-fold degenerate sites, which are largely neutral and exhibit remarkable clock-like behavior [31,32].

To address this phylogenetic challenge, we selected 16 representative fungi (9 Orbiliomycetes, 3 Pezizomycetes, 2 Eurotiomycetes, 1 Saccharomycetes, and 1 Taphrinomycetes) that contain the *Ao415* gene cluster, along with 1 fungus from Cystobasidiomycetes, which lacks the *Ao415* gene cluster, as an outgroup. We identified 1,136 sets of 1:1 orthologous protein-coding genes across these 17 fungal species and reconstructed a well-supported genome-wide phylogeny based on 1,141,520 concatenated amino acid positions (Fig. S5a). Robust phylogenomic trees based on various codon positions were also generated (Fig S5b,c). Although the topologies of these phylogenetic trees were consistent and well-supported, significant discordance was observed in the topologies of single-gene trees (Fig. S6). Such incongruence is often caused by incomplete lineage sorting (ILS), a common issue in the phylogenies of many animal groups that complicates phylogenetic inference [33]. To ensure the robustness of the reconstructed phylogeny despite ILS, we employed ASTRAL-III for a coalescent-based phylogenetic analysis using 1,136 orthologous gene trees. The topology of the resulting ASTRAL coalescent tree (Fig. S5d) is identical to the genome-wide tree and aligns with the branching order of major groups estimated in previous studies [13]. Our analysis further confirms that *Dactylella cylindrospora* is the closest extant relative of NTFs within Orbiliomycetes. This finding provides an excellent opportunity to identify the critical evolutionary forces associated with the origin of trapping devices during the early evolution of carnivorous fungi.

A time-calibrated phylogenetic tree, constructed using 275,133 four-fold degenerate sites from 1,136 single-copy orthologous genes and calibrated with three major events [28]: Ascomycota crown group (487–773 Mya), Orbiliomycetes–other Pezizomycotina (353–554 Mya), Saccharomycotina crown group (276–514 Mya), and one fossil calibration point (node 9: >100 Mya) [29], indicated that the fungal lineage containing the *Ao415* cluster originated approximately 517 Mya (95% confidence interval (CI): 493.64−555.41 Mya). This timing aligns with a significant increase in ironstone during the early Ordovician (Fig. 5c). Furthermore, carnivorous fungi with trapping devices are estimated to have diverged from their saprophytic relatives (*Dactylella cylindrospora*) around 258 Mya (CI: 231−287 Mya). We did not find a correlation between the distribution patterns of iron (using the number of ironstones as a proxy) over geological time and the origin of trapping devices in NTFs.

Both our time-calibrated tree and previous studies suggest that the origin of trapping devices in NTFs coincided with the Permian-Triassic mass extinction. There is considerable evidence indicating that abrupt climate changes, including both warming and cooling, have been linked to mass extinction events throughout Earth's history [34–36]. Specifically, a sharp increase in global temperatures is associated with the Permian-Triassic mass extinction. During this period, sea surface temperatures reached approximately 40 °C, with land temperatures likely fluctuating to even higher values [36]. Mapping the changes in global average temperatures throughout the Phanerozoic [37] onto the evolutionary trajectory of carnivorous fungi reveals that the divergence of species with trapping devices coincided with lethally high temperatures during the early Triassic Greenhouse (Fig. 5c).

Notably, before the emergence of this NTF group, the ancestor of Orbiliomycetes experienced the longest ice age, known as the Late Paleozoic Ice Age (from 360 to 255 Mya) [38,39]. During this period, the five crucial genes (encoding noranthrone synthase, siderophore biosynthesis acetylase, ferric-chelate reductase, metalloreductase, and CccA) involved in iron storage and sequestration were lost (S8 Fig). Additionally, the emergence of the *Ao415* gene cluster occurred during a period of high temperatures in the Cambrian (Fig. 5c). Therefore, we hypothesize that the development of nematode-trapping structures in NTFs was an adaptation to high-temperature environments after loss of five pivotal iron related gene during the longest-lived ice age.

Temperature-dependence of trapping devices and iron compositions in *A. oligospora* mycelia

To date, the role of temperature changes in the development of trapping devices remains poorly understood. While many studies suggest that temperature influences fungal mycelial growth, we specifically evaluated the growth of *A. oligospora* WT and the mutant Δ*Ao414* on PDA at five different temperatures: 32°C, 28°C, 24°C, 20°C, and 16°C. Both WT and Δ*Ao414* exhibited the largest colony growth at 24°C and smaller colony growth at 28°C compared to 20°C. Importantly, both strains failed to grow at 32°C but were able to grow at 16°C. These observations indicate that *A. oligospora* is sensitive to high temperatures, with an optimal growth temperature of 24°C (Fig. 6a). Further comparisons of WT and Δ*Ao414* strains cultivated at 28°C, 20°C, and 12°C revealed that both strains could still grow at 12°C. Notably, we observed significant temperature-dependent development of trapping devices in both WT and Δ*Ao414* strains (Fig. 6b).

Recent studies suggest that temperature variations can influence free iron content and trigger metabolic changes in thermophilic fungi [8,40]. We hypothesized that iron might play a key role in the temperature-dependent development of trapping devices in *A. oligospora*. To investigate this, we compared the iron levels and ratios in the mycelia of both WT and mutant Δ*Ao414* strains at three different temperatures: 28°C, 20°C, and 12°C. We observed that the Δ*Ao414* mutant spontaneously developed numerous trapping devices at 28°C, which may account for the low ferric levels in Δ*Ao414* mycelia at this temperature (Fig. 6c). At 20°C and 12°C, the Δ*Ao414* mutant exhibited significantly higher ferric levels compared to WT, consistent with its inability to synthesize desferriferrichrome for ferric sequestration (Fig. 6c). Consequently, the Δ*Ao414* mutant had an extremely low iron ratio of ferrous to ferric iron at these temperatures compared to WT. Notably, the Δ*Ao414* mutant displayed opposite temperature dependent iron ratios of ferrous to ferric iron compared to WT. WT showed the highest levels of ferrous and total free iron, as well as the highest iron ratios of ferrous to ferric iron, at 12°C, with an opposite trend observed at 28°C (Fig. 6d). This indicates that iron content in WT mycelia is negatively correlated with temperature.

Discussion

The ability to isolate and temporarily store unwanted components to adapt to environmental changes is a fundamental aspect of homeostasis regulation in all living organisms. Hemochromatosis is a disorder characterized by iron overload resulting from inherited or acquired factors [41, 42]. If left untreated, excess iron can damage various organs, including the liver, heart, pancreas, endocrine glands, and joints, potentially leading to cirrhosis, liver failure, cancer, arthritis, diabetes, and heart failure [41]. Caucasians are particularly susceptible to developing iron overload and the associated complications of hemochromatosis due to a higher prevalence of mutations in the homeostatic iron regulator gene within this population, which leads to excessive iron absorption [43, 44]. Recent research has increasingly focused on discovering new molecules and mechanisms for managing iron, controlling its availability, and mitigating its intrinsic toxicity to improve treatments for iron overload.

In the fungal kingdom, vacuolar iron storage is the primary mechanism for iron detoxification, surpassing siderophore-mediated storage due to its capacity to sequester iron [45,46]. In *Saccharomyces cerevisiae*, iron is imported into the vacuole by the transporter Ccc1 for storage, reuse, and detoxification as ferric polyphosphate [20]. Inactivation of the *Ccc1* homolog, *CccA*, in the human pathogenic fungus *Aspergillus fumigatus* significantly reduces resistance to iron toxicity [21]. Ccc1- or CccA-mediated vacuolar iron detoxification is especially critical for pathogenic fungi, which must adapt to grow inside warm-blooded hosts [4,47,48]. Given the importance of vacuolar iron storage, one might wonder if alternative forms of iron storage exist to cope with iron overload when encountering vacuolar dysfunction. Temperature is a paramount environmental and climatic selective force that influences morphological changes and biological processes, affecting vital physiological and cellular functions [49-53]. However, the interplay between iron overload, storage mechanisms, and temperature remains largely unexplored.

In this study, we found that high temperatures significantly contribute to triggering iron excess in the NTF *A. oligospora*. Our results showed that *A. oligospora* WT mycelia exhibited significantly lower total iron levels and a reduced ratio of ferrous to ferric iron at high temperatures compared to lower temperatures. This observation is consistent with recent research indicating that cold stress significantly increases both total iron levels and the ratio of ferrous to ferric iron in the mycelia of thermophilic fungi such as *Thermomyces* species [40]. This suggests a negative correlation between temperature and iron content in fungal mycelia. It is reasonable to conclude that *A. oligospora* has adapted to low temperatures by accumulating higher total iron content to support energy production. Conversely, in response to high temperatures, the fungus reduces iron levels by developing trapping devices for excess iron sequestration, which serves as a key strategy for climate adaptation.

We observed that reducing the temperature or supplementing with desferriferrichrome significantly inhibits the development of trapping devices in *A. oligospora*. Conversely, iron supplementation or a deficiency in desferriferrichrome biosynthesis triggers extensive formation of trapping devices. Notably, the electron-dense bodies within these trapping devices are less efficient for iron storage and isolation compared to desferriferrichrome-mediated ferrichrome granules, but more efficient than

mitochondria and vacuoles, serving as an alternative iron storage system. A previous study reported that electron-dense bodies in the alga *Cyanidium caldarium* also function in iron storage [54]. This suggests that the role of electron-dense bodies in iron sequestration may be a widespread phenomenon rather than specific to a single fungal strain. The key difference between *A. oligospora* and *Cyanidium caldarium* is that the fungus develops specialized mycelial structures—trapping devices—to house these electron-dense bodies. The development of trapping devices is considered a diagnostic marker for the transition from a saprophytic to a predatory lifestyle in NTF and plays a crucial role in their carnivorous activity.

This study first highlights temperature as a crucial non-nutrient environmental factor influencing trapping device development in *A. oligospora* through its regulation of iron homeostasis. Historically, nutrient signals have been considered the primary triggers for the formation of trapping devices [55]. However, the role of temperature in this process has been relatively underexplored, despite its significant impact on fungal phenotype and diversity. Recent phylogenetic analyses of the protein *Ao415* suggest that NTFs are closely related to species such as *Kalaharituber pfeilii* (a desert truffle), *Tricharina praecox* (cup fungus), *Trichophaea hybida* (cup fungus), *Morchella sextelata* (true morel), *Morchella importuna* (true morel), *Choiromyces venosus* (a truffle), and *Tuber borchii* (a truffle) [8]. Many of these fungi produce valuable and edible fruiting bodies. Our findings suggest that the development of trapping devices in *A. oligospora* serves as a climate adaptation strategy for sequestering excess iron under high temperatures. This insight may help elucidate the mechanisms underlying fruiting body formation in these economically and ecologically significant fungi.

In summary, we have identified temperature as a critical non-nutrient environmental factor that triggers excess iron accumulation and the development of trapping devices in *A. oligospora*. These trapping devices represent unique iron storage structures that sequester excess iron from the mycelia to mitigate the effects of high temperatures. Unlike known iron sequestration granules or organelles within cells, these trapping devices are distinct morphological structures that differentiate from the mycelia. The electron-dense bodies within the trapping devices serve as the primary granules for iron sequestration. These iron-sequestering structures offer a novel prototype for microbial iron systems. Consequently, NTFs provide a valuable eukaryotic model for developing innovative agents and therapies for treating iron overload-associated diseases.

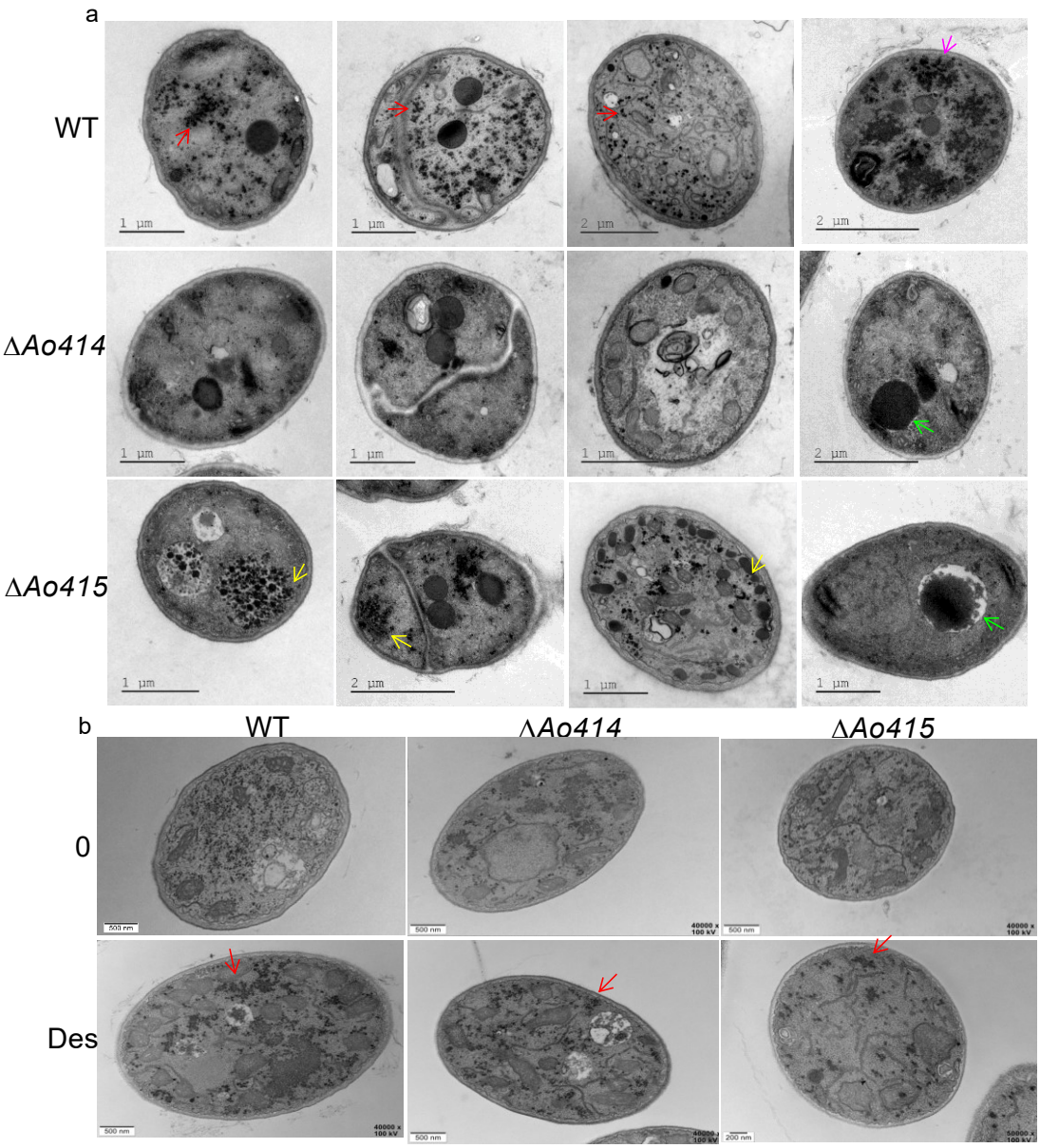

Fig 1. **TEM analysis of cellular changes in the fungal mycelia of *A. oligospora* in response to the loss and supplementation of desferriferrichrome.** *ΔAo414* is deficient in the entire desferriferrichrome biosynthetic pathway, while *ΔAo415* lacks only part of this pathway, specifically still producing desferriferrichrome precursors capable of iron chelation. **a**, Comparison of organelles in the mycelial cells of WT, Δ*Ao414* and Δ*Ao415*. Red arrow: normal ferrichrome granules. Yellow arrow: abnormal ferrichrome granules. Green arrow: autophagosomes. **b**, The effect of desferriferrichrome on organelles in mycelial cells of WT, Δ*Ao414* and Δ*Ao415*. Des: desferriferrichrome solution. 0: solvent as control.

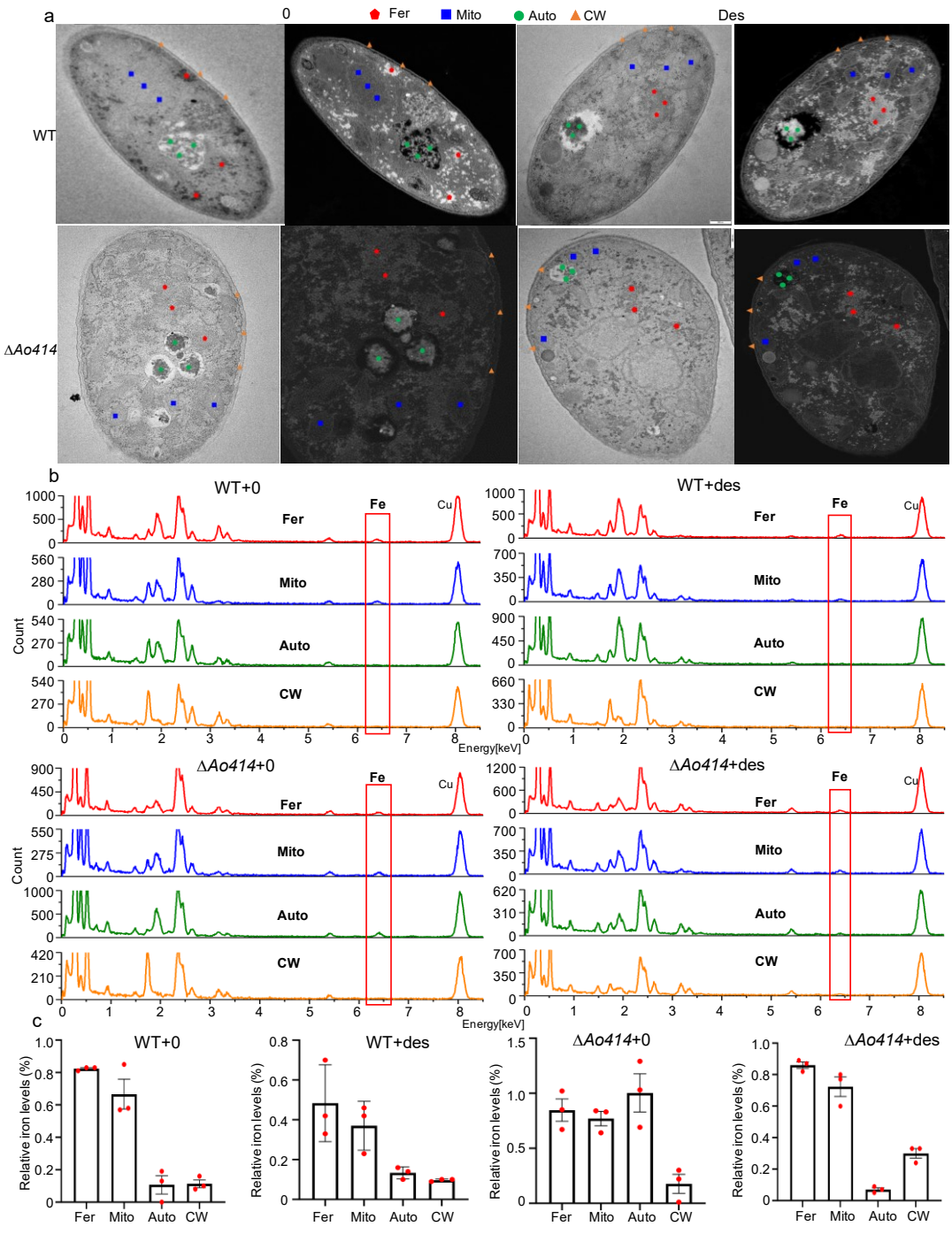

Fig 2. **Evaluation of the functions of desferriferrichrome in iron distribution and storage in *A. oligospora* mycelia.** Des: desferriferrichrome solution. 0: solvent as control. **a**, TEM image and TEM-EDX electronic micrograph of mycelia of WT and mutant Δ*Ao414* treated with and without desferriferrichrome, with analysis sites marked by different color indicators. Fer: ferrichrome. Auto: autophagosomes. Mito: mitochondria. CW: cell walls. **b**, X-ray spectra of different organelles within the same mycelial cell of WT and mutant Δ*Ao414*, treated with and without desferriferrichrome. **c**, Comparison of relative iron levels in different organelles within the same mycelial cell of WT and mutant Δ*Ao414*, treated with and without desferriferrichrome.

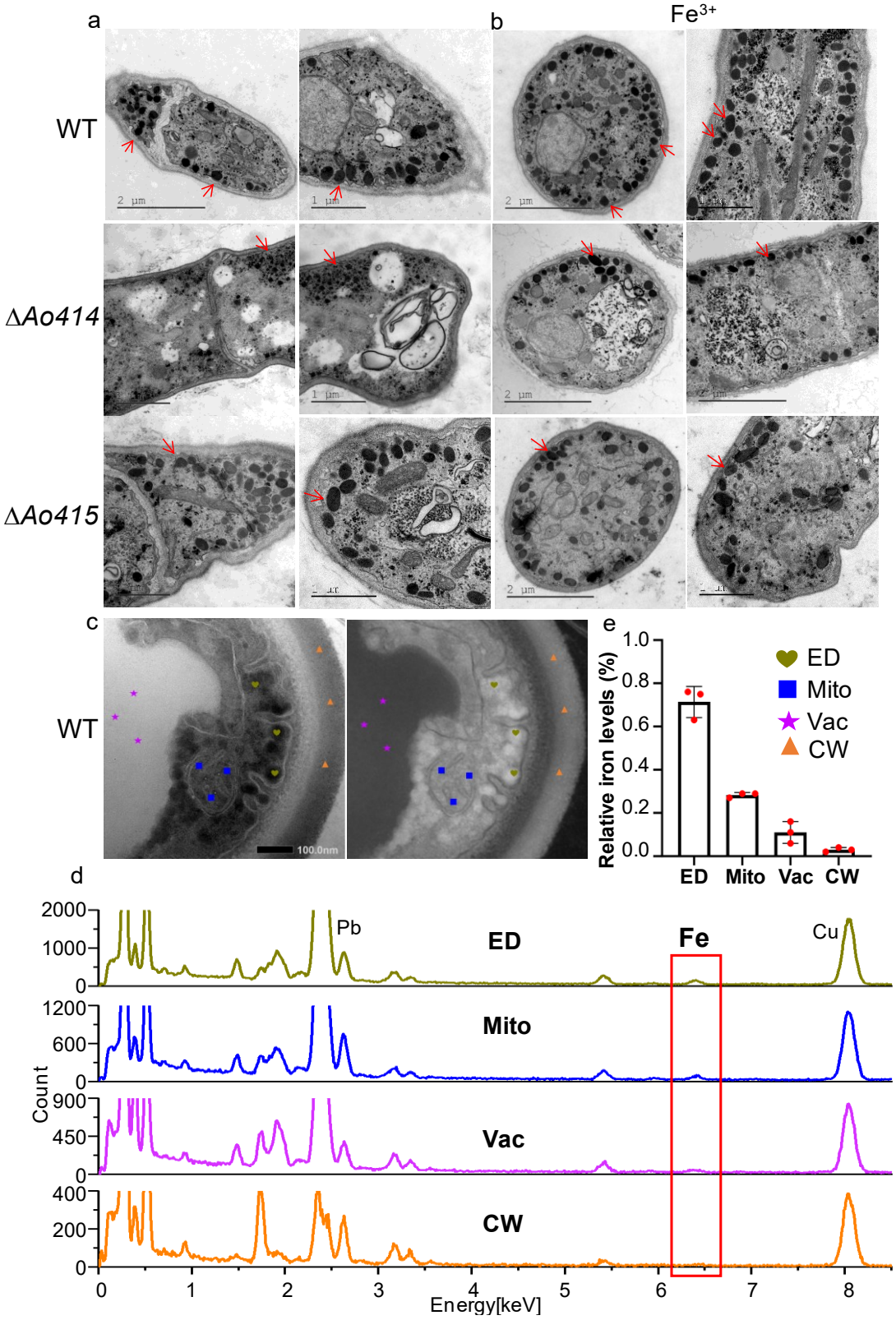

Fig 3. **Evaluation of desferriferrichrome functions in the organelles and iron distribution in the trapping devices of *A. oligospora*. a**, TEM analysis of the organelles in trapping devices from WT, Δ*Ao414* and Δ*Ao415*. Red arrow: electron dense body. **b**, TEM analysis of the organelles in trapping devices from WT, Δ*Ao414* and Δ*Ao415* treated with 30μM ferric solution. Red arrow: electron dense body. **c**,

TEM image and TEM-EDX electronic micrograph of WT trapping devices, with analysis sites marked by different color indicators. ED: electron dense body. Mito: mitochondria. Vac: Vacuole. CW: cell walls. **d**, X-ray spectra of different organelles within the same cell of WT trapping device. **e**, Comparison of relative iron levels in various organelles within the same cell of WT trapping devices.

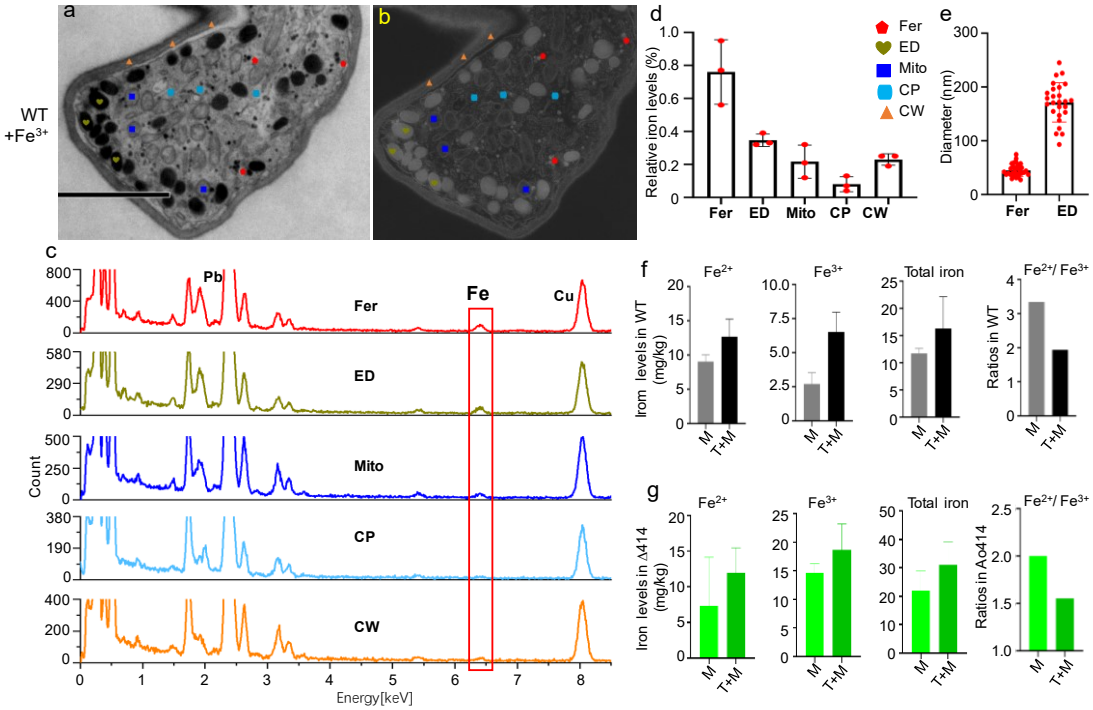

Fig 4. **Comparison of iron storages between ferrichrome organelles and electron dense bodies in *A. oligospora* WT treated with ferric. a, b,** TEM image (**a**) and TEM-EDX electronic micrograph (**b**) of WT trapping device, with analysis sites marked by different color indicators. Fer: Ferrichrome. ED: electron dense body. Mito: mitochondria. CP: cytoplasm. CW: cell walls. **c,** X-ray spectra of different organelles within the same cell of WT trapping device. **d,** Comparison of relative iron levels in various organelles within the same cell of WT trapping device. **e,** Comparison of sizes between ferrichrome organelles and electron dense bodies in *A. oligospora*. **f,** Comparison of ferrous, ferric and total iron levels, as well as the ratios of ferrous to ferric iron between mycelia (M) and trapping devices (T) in WT. **g,** Comparison of ferrous, ferric and total iron levels, as well as the ratios of ferrous to ferric iron between mycelia (M) and trapping devices (T) in the mutant Δ*Ao414*.

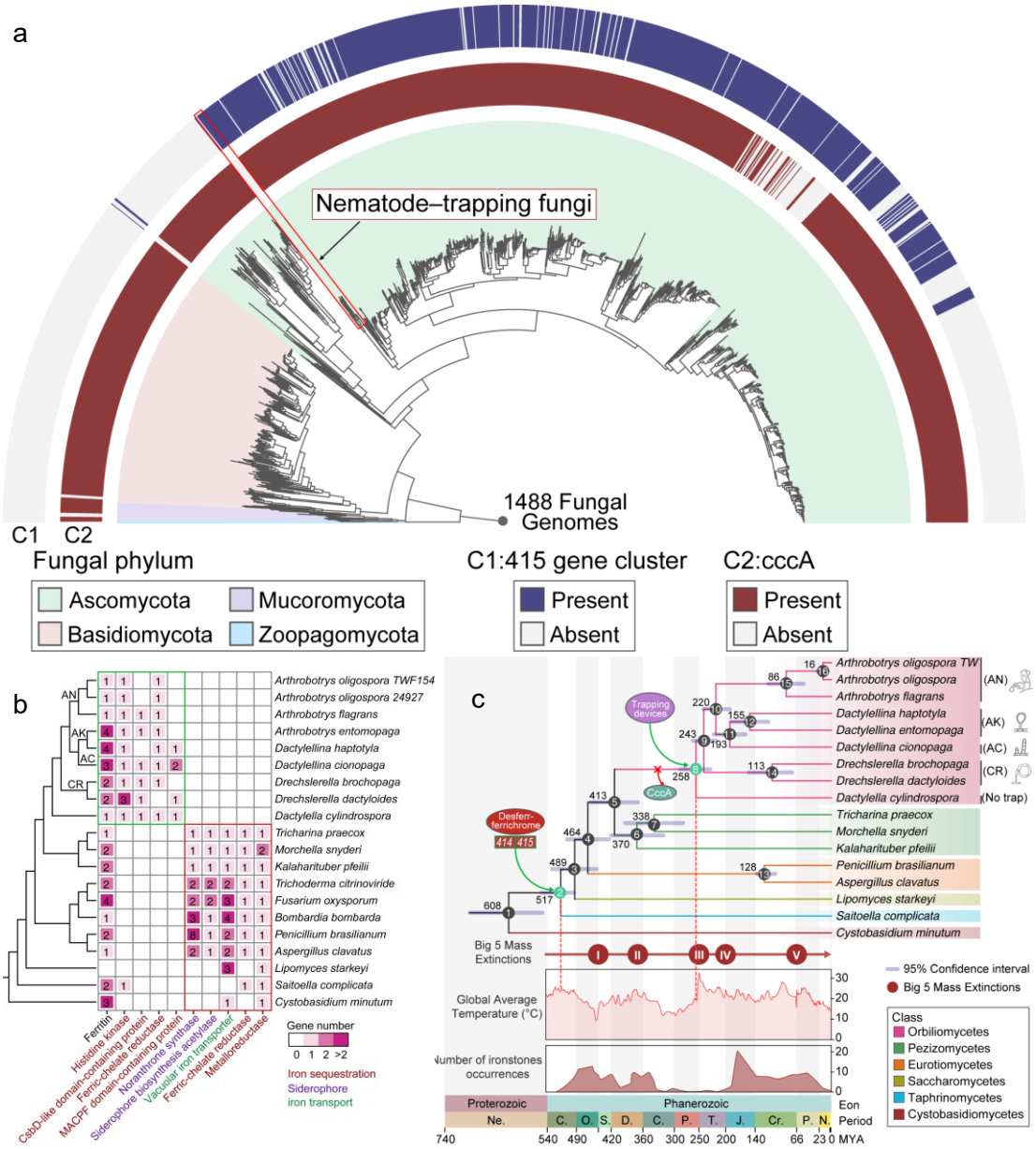

Fig 5. **Phylogeny and time-scale evolution analysis of fungal group with trapping devices in Ascomycota. a**, Distribution patterns of the *Ao415* gene and the vacuole transport gene *cccA* in fungi kingdom. This panel highlights the presence and absence of these genes in fungal genomes. **b**, Heatmap illustrating the gain and loss of genes involved in iron sequestration and transport in NTFs, including ferritin, histidine kinase, CsbD-like domain-containing protein, ferric-chelate reductase, MACPF domain-containing protein, noranthrone synthase, siderophore biosynthesis acetylase, vacuolar iron transporter, ferric-chelate reductase and metalloreductase. The copy numbers of each gene are indicated in each color block. The tree topological structure is derived from the tree shown in panel A. **c**, Estimated divergence times of major lineages in the carnivorous Orbiliomycetes, with inferred occurrences of Phanerozoic ironstones and Phanerozoic global average temperature (GAT) trends. The chronogram was constructed using MCMCTree in the PAML package with 275,133 four-fold degenerate sites from 1136 single copy orthologous genes. Calibration was based on three major events [28]: Ascomycota crown group (487–773 Mya), Orbiliomycetes–other Pezizomycotina (353–554 Mya), Saccharomycotina crown

group (276–514 Mya) and one fossil calibration point (node 9: >100 Mya) [29]. Error bars represent the 95% highest posterior density (HPD) of node ages. Numbered circles at each node indicate node sequence from root to leaves, and node ages are shown. Circles labeled with Roman numerals represent major Phanerozoic mass extinction events: Late Devonian (375 Mya), Permian-Triassic (251.4 Mya), Triassic-Jurassic (201.4 Mya), and Cretaceous-Paleogene (66 Mya). Time periods are abbreviated as follows: De: Devonian, Ca: Carboniferous, Pe: Permian, Tr: Triassic, Ju: Jurassic, Cr: Cretaceous, P: Paleogene, N: Neogene.

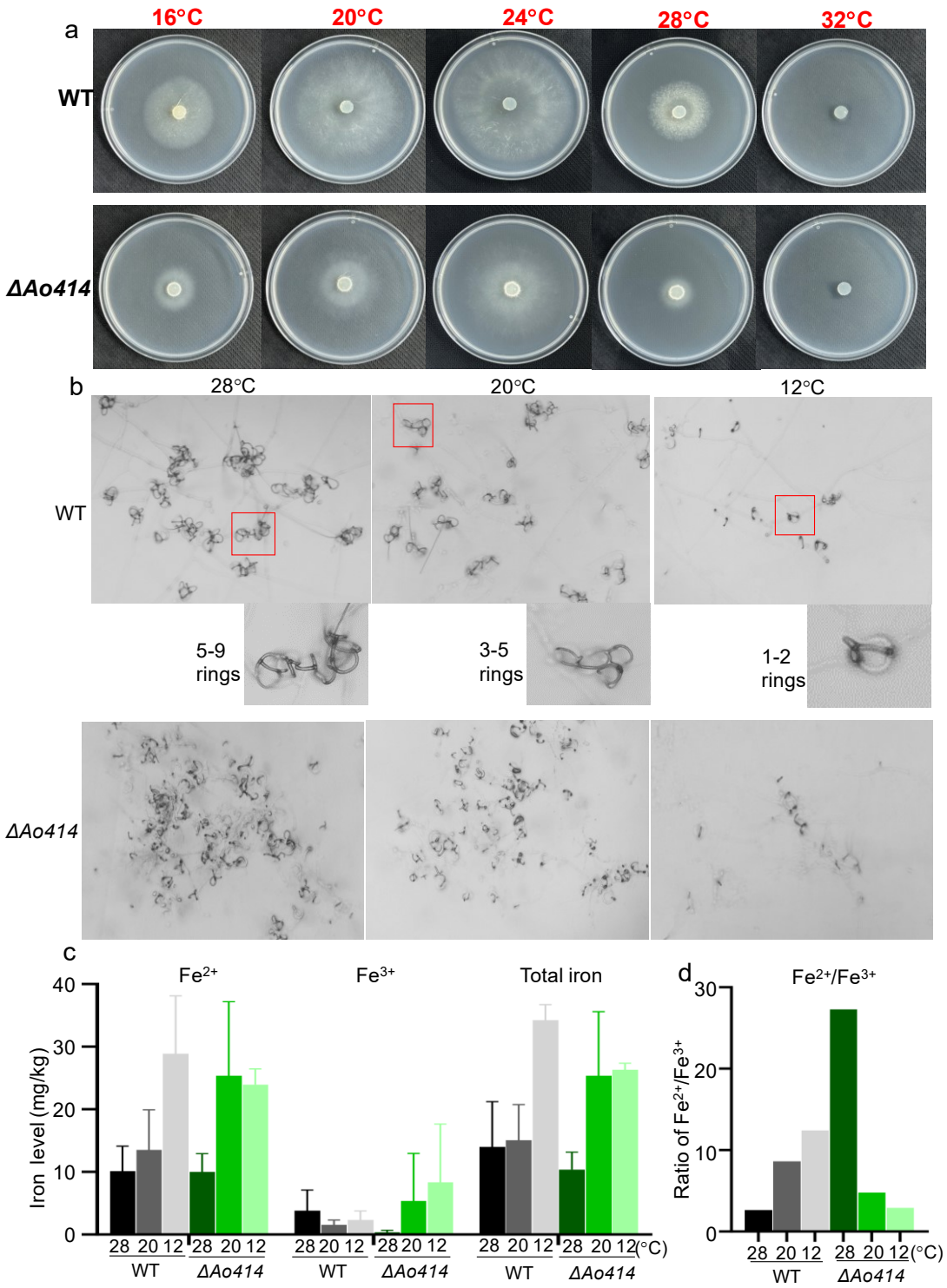

Fig 6. Evaluation of the role of temperatures on colony growth, trapping devices, iron levels, and iron ratios in *A. oligospora*. a, The effect of temperature on colony growths in *A. oligospora* WT and the mutant Δ*Ao414* at 32°C, 28°C, 20°C, 24°C, and 16°C. **b,** Comparison of trapping devices in WT and the mutant Δ*Ao414* at temperatures of 28°C, 20°C, and 12°C. **c,** The effect of temperature on iron levels in fungal mycelia of WT and the mutant Δ*Ao414*. **d,** The effect of temperature on iron ratios in fungal mycelia of WT and the mutant Δ*Ao414*.

541

Materials and Methods

Fungal strains and cultivation

YMF1.01883 (ATCC 24927) was procured from the State Key Laboratory for Conservation and Utilization of Bio-Resources and was cultivated at 25 °C for 3 to 4 days on a 9 cm Petri dish containing PDA (potato 200 g/L, glucose 10 g/L, agar 15 g/L, ddH_2O or tap water). Subsequently, 9 mm discs of the fungal colonies were transferred to 9 cm Petri dishes containing YMA (2 g/L yeast extract, 10 g/L maltose, agar 20 g/L) and incubated at 25 °C for 6 to 7 days. The spores were then washed with 20 mL of 0.05% Tween-80 mixed with approximately 3 mm glass beads.

Generation of gene deletion mutants

A modified homologous recombination method was employed to construct the mutants Δ*Ao414* and Δ*Ao415*. The upstream and downstream homologous arms of the target gene were cloned from *A. oligospora* YMF1.01883, and the *HygR* resistance sequence was cloned from a PUC19-1300-D-HYB vector using the Prime STAR Max enzyme (TsingKe, Beijing, China). All primers used in this study are listed in S1 Table. The DNA fragments (5′ flank, hygromycin B, and 3′ flank) were purified using the RiboEXTRACT Universal DNA Purification Kit (Tsingke, China). The purified 5′ flank DNA fragment was inserted into the enzyme-digested PUC19-1300-D-HYB vector using the In-Fusion method to produce a PUC19-1300-D-HYB-5′ vector. Subsequently, the 3′ flank DNA fragment was inserted into this vector to generate a PUC19-1300-D-HYB-5′-3′ vector. The homologous fragment was amplified and purified as previously described. *A. oligospora* protoplasts were prepared as previously described. The purified homologous fragment was transformed into *A. oligospora* protoplasts. Transformation colonies were selected after incubation at 28 °C for 2−4 days, and each colony was transferred to a new plate containing PDA. After incubation at 28 °C for 5 days, genomic DNA of putative transformants was extracted and verified by polymerase chain reaction (PCR) to check for the integration of the target gene into the genome. Mutants deficient in the target gene were screened by PCR and confirmed by sequencing analysis. Further confirmation of the mutants was performed by Southern blot hybridization using the North2South Chemiluminescent Hybridization and Detection Kit according to the manufacturer's instructions (Pierce, Rockford, IL). For Southern blot analysis, restriction enzyme HindIII was used to digest WT and Δ*Ao414* genomic DNA, and restriction enzyme SmaI was used to digest WT and Δ*Ao415* genomic DNA (S1 Fig).

Development of trapping device

To facilitate the collection of mycelia, *A. oligospora* YMF1.3170 was cultured at 25 °C for 3 to 4 days on 9 cm Petri dishes containing potato dextrose agar (PDA) with cellophane (4 cm diameter, area 50.24 cm^2). *Caenorhabditis elegans* N2 was grown in a 250 mL flask with oatmeal agar medium (oatmeal 30 g, water 20 mL) for 7 days. The nematodes were then collected from the flask's walls and transferred to a 2 mL microcentrifuge tube [56]. To prepare the nematode suspension, 1 mL of double-distilled water was added and mixed. The nematode concentration was subsequently adjusted to 300 nematodes per 200 μL for the assay. The wild-type (WT) and mutant strains were exposed to 200 μL of double-distilled water containing 300 nematodes to induce the formation of trapping devices, classified as the mycelia + trapping devices (M+T) group. The control group, which only included mycelia (M), was treated with 200 μL of double-distilled water without nematodes.

592
593 **Desferriferrichrome assay**
594 Five milligrams of desferriferrichrome (CAS No. 34787-28-5, Sigma Co.) were
595 dissolved in 5 mL of dimethyl sulfoxide (DMSO) to prepare a 1 mg/mL
596 desferriferrichrome stock solution. To achieve a final concentration of 1.45 μM
597 desferriferrichrome, 150 μL of the 1 mg/mL stock solution was added to 150 mL of
598 potato dextrose broth (PDB). Wild-type (WT) and mutant strains, cultured on potato
599 dextrose agar (PDA) for 7 days, were inoculated into potato dextrose (PD) broth (200
600 g/L potatoes, 20 g/L glucose) and incubated on a shaker at 180 rpm for 12 hours. The
601 culture was then supplemented with 1.45 μM desferriferrichrome and further
602 incubated on the shaker for another 12 hours. The mycelia were harvested, fixed with
603 2.5% glutaraldehyde, and examined using transmission electron microscopy (TEM).
604
605 **Fe^{3+}Assay**
606 The fungal strains were initiated with 9 cm diameter hyphal disks at 28°C for 6 days on
607 the plates of PDA supplemented with or without $FeCl_3 \cdot 6H_2O$ (10–30 μM) and then
608 about 400 nematodes were introduced to the cultures. After 12 h, traps and captured
609 nematodes per plate were observed under a microscope and counted at specific
610 time-points. The diameter of each colony was measured and then calculated with
611 GraphPad 9.3.4.
612
613
614 **Iron contents**
615 An iron assay kit (#ab83366, Abcam) was used to evaluate intracellular iron levels
616 (Fe^{2+} and Fe^{3+}) in fungi [40]. First, mycelia (20–80 mg) were collected in
617 phosphate-buffered saline (PBS) containing 80 g NaCl, 2 g KCl, 14.4 g Na_2HPO_4, and
618 2.4 g KH_2PO_4 in 1 L of double-distilled water. The mycelia were then homogenized in
619 iron assay buffer using a Dounce homogenizer on ice with 50–100 passes. Next, iron
620 reducer was added to the collected supernatant, mixed, and incubated. Following this,
621 iron probe (3-(2-Pyridyl)-5,6-bis(5-sulfo-2-furyl)-1,2,4-triazine, disodium salt) was
622 added, mixed, and incubated for 1 hour. The resulting solution was immediately
623 measured using a microplate reader at OD = 593 nm. To account for the effects of
624 nematodes on iron content in the mycelia + trapping devices (M+T) groups,
625 nematodes were removed from the M+T samples using a 10 μL pipette. Additionally,
626 the iron content of 300 nematodes was measured separately. Iron content in the M+T
627 groups, both with and without nematodes, was evaluated using the same method. All
628 mycelia were collected, weighed, and suspended in double-distilled water at a 1:10
629 ratio. The suspension was ground using an ultrasonic cell disruptor to obtain a
630 uniform mixture, from which 1 mL was taken for analysis. Similarly, 300 nematodes
631 were suspended in 1 mL of distilled water, ground using an ultrasonic cell disruptor,
632 and then centrifuged at 16,000 rpm for 10 minutes to separate the supernatant for
633 further experiments.
634
635 **Transmission electron microscopy (TEM)**
636 For transmission electron microscopy (TEM) analysis, ultrathin sections of hyphal
637 cells were prepared and examined as previously described [40]. The samples were
638 pretreated with 4% paraformaldehyde and then incubated overnight at 4 °C with 2.5%
639 glutaraldehyde (Sigma) in phosphate buffer (pH 7.4). Following this, the samples
640 were post-fixed in 1% osmium tetroxide (OsO_4). They were then dehydrated through
641 a gradient ethanol series, embedded in Spurr resin, and stained with 2% uranyl acetate

642 and Reynold's lead citrate. Finally, the samples were examined using an H-7650
643 transmission electron microscope (Hitachi, Tokyo, Japan).
644
645 **Transmission electron microscopy-energy dispersive X-ray spectroscopy**
646 **(TEM-EDX)**
647 The distributions of elements within the samples were qualitatively determined
648 according to the method conducted by Sheraz et al. [57]. In detail, the mycelia or
649 trapping devices were placed in a primary fixative consisting of 2.5% (v/v)
650 glutaraldehyde for approximately 6 hours at 4 °C. The samples were then washed
651 three times at 15-minute intervals with phosphate-buffered saline (PBS) buffer (0.1
652 mol/L, pH 6.8), followed by post-fixation in 1% (m/v) osmium tetroxide for 2 hours
653 at 4 °C. After washing with PBS buffer, the samples were dehydrated through a
654 graded ethanol series: 30% (v/v) for 15 minutes, 50% (v/v) for 15 minutes, 70% (v/v)
655 for 15 minutes, 80% (v/v) for 15 minutes, 90% (v/v) for 15 minutes, and 100% (v/v)
656 for 15 minutes, twice. Prior to embedding, the samples were infiltrated with a mixture
657 of anhydrous ethanol and epoxy resin EPON-812 (1:1, v/v) overnight. The samples
658 were then placed in an oven at 60 °C for 48 hours and finally stored in desiccators.
659
660 Structures were further sectioned into ultrathin slices using an ultramicrotome (Leica
661 RM2016, Germany). The resulting 100-nm ultrathin sections were mounted on
662 200-mesh copper TEM grids (Agar Scientific). Where indicated, sections were stained
663 with 1% uranyl acetate for 15 minutes, followed by Reynold's lead citrate (Reynolds,
664 1963) for 7 minutes. Samples were then observed using a JEOL 1400 transmission
665 electron microscope (JEOL, Akishima, Japan) at 80 kV. To qualitatively determine the
666 distribution of elements within the samples, stained sections were analyzed to identify
667 Fe deposits and quantify Fe content through X-ray microanalysis. Energy dispersive
668 X-ray spectroscopy (EDAX, USA), equipped with the TEM, was employed for this
669 purpose. Circular regions of interest were selected for energy-dispersive X-ray (EDX)
670 analysis. An electron beam with an acceleration voltage of 200 kV and a spot size of
671 10 nm was focused on the specimen, and X-ray spectra were collected for
672 approximately 100 seconds. X-rays were detected using an Oxford INCAx-sight
673 detector (Oxford Instruments, Abingdon, UK) and analyzed with the Oxford INCA
674 SUITE v.4.02. The Zeta factor method was used for standardless quantitative analysis,
675 checking elements manually selected and reporting elements excluded from
676 qualitative analysis.
677
678 **Genome data collection and quality assessment**
679 To investigate the distribution of a genomic element within the fungal kingdom, we
680 downloaded all published genome and corresponding annotation files from the JGI
681 Mycocosm database (15 December 2022). Additionally, we used "Orbiliomycetes" as
682 a search term in NCBI's Genome Browser to retrieve all genome assemblies with
683 gene annotation files for this class. In total, 2,175 fungal genomes were collected. For
684 each predicted gene, the longest transcript was extracted as the representative
685 transcript. Protein sequences for each genome were generated using gffread (v.0.9.12)
686 [58]. To assess the quality of the gene sets for use in phylogenomic analyses, we
687 evaluated their completeness using Benchmarking Universal Single-Copy Orthologs
688 (BUSCO) (v.3.0.2) [59] based on the fungi_odb10 lineage dataset (2021-06-28).
689 Genes were categorized as "single copy" if only one complete predicted gene was
690 present in the genome, "duplicated" if two or more complete predicted genes were
691 found for one BUSCO gene, "fragmented" if the predicted gene was shorter than 95%

of the aligned sequence lengths from 50 different fungal species, and "missing" if no predicted gene was present. Only genomes with a BUSCO completeness of 90% or higher were considered high-quality and retained. In total, 1,488 high-quality fungal genomes were retained (1,177 Ascomycota; 289 Basidiomycota; 21 Mucoromycota; 1 Zoopagomycota), representing 1,229 species: Ascomycota (n=996), Basidiomycota (n=233), Mucoromycota (n=19), and Zoopagomycota (n=1) (S3 Table).

Screening of iron sequestration, transports, and siderophore related genes

Genes classified as having ferric-chelate reductase activity (GO:0000293) were considered to be involved in iron sequestration. Genes associated with iron ion transmembrane transport (GO:0034755) were identified as involved in iron transport. Genes categorized under siderophore biosynthetic process (GO:0019290), siderophore metabolic process (GO:0009237), and siderophore transport (GO:0015891) were deemed to be involved in siderophore-related processes. Additionally, ferritin, a common iron storage protein, was also included.

Identification homologue of *Ao415* biosynthetic gene cluster in the fungal kingdom

The biosynthetic gene clusters for each genome were annotated using antiSMASH 7.0 (v.7.0.0) [60] via the command-line version with default parameters, except for the argument '--taxon fungi'. In total, 67,350 secondary metabolism gene clusters were annotated from 1,488 fungal genomes. A local database was created from GenBank sequences of all gene clusters using the 'cblaster makedb' module (v.1.3.18) [61]. To identify gene clusters homologous to the *Ao415* gene cluster within the fungal kingdom, the search function of cblaster was employed to query the amino acid sequences of the seven genes in the *Ao415* gene cluster (Ao410–Ao416) against the local database. Both *Ao414* and *Ao415* needed to be represented in a hit cluster, and the minimum percent identity for a BLAST hit was set to 30%. We identified 744 fungal genomes containing *Ao415* gene cluster homologues, all of which were from Ascomycetes. The presence and absence of the *Ao415* gene cluster were mapped onto a phylogenetic tree (containing 1,488 high-quality fungal genomes) extracted from the MycoCosm portal to visualize the distribution of the *Ao415* gene cluster within the fungal kingdom.

Inference of homologous groups

To better understand the evolutionary trajectory of the *Ao415* biosynthetic gene cluster within the fungal kingdom, we selected 17 representative fungi (9 Orbiliomycetes, 3 Pezizomycetes, 2 Eurotiomycetes, 1 Saccharomycetes, and 1 Taphrinomycetes) containing the *Ao415* gene cluster, as well as 1 fungus from Cystobasidiomycetes lacking the *Ao415* gene cluster, to serve as an outgroup. This selection was guided by the fungal species tree from the MycoCosm portal. Protein sequences from these 17 fungal genomes, totaling 131,694 sequences, were subjected to all-versus-all BLASTP (v.2.11.0+). The resulting output was then analyzed using OrthoFinder (v.2.5.2) [62] for gene family clustering, employing the MCL algorithm with an inflation factor set to 1.5. This analysis identified 1,136 sets of 1:1 orthologous protein-coding genes.

Function annotations of homologous groups

To assign function annotations to each homologous group (OG), we selected a representative sequence for each group. First, we ordered the sequences within each

OG by their lengths using the 'sortbylength' option in USEARCH11 (v.11.0.667) [63]. Next, we employed the UCLUST algorithm to cluster the sequences within each OG based on 30% amino acid sequence similarity. The sequence with the highest abundance in each OG was designated as the representative sequence. In cases of equal abundance, the longest sequence was chosen as the representative. For each representative sequence, gene function and gene ontology (GO) were predicted using the PANNZER2 web server [64].

Phylogenetic analyses and divergence times estimating

Amino acid sequences for each orthogroup were aligned using MAFFT (v.7.505) with the 'auto' parameter. Codon alignments were generated from these MAFFT-aligned amino acid sequences using PAL2NAL (v14) with default parameters. The aligned amino acid sequences and their corresponding codon alignments were concatenated to construct amino acid (AA) and nucleotide (NT) data matrices, respectively. For the AA data matrix, the best substitution model was determined using the "-m TEST" parameter, which estimates the optimal model based on Bayesian Information Criterion (BIC) values. Maximum likelihood (ML) trees with 1,000 bootstrap iterations were constructed according to the best-fitting model using IQ-TREE2 [65]. Fourfold degenerate sites were extracted from the NT data matrix using the open-source tool get4foldSites (https://github.com/brunonevado/get4foldSites). Divergence times for all nodes were estimated with MCMCTree from the PAML package, using 275,133 fourfold degenerate sites from 1,136 single-copy orthologous genes. Calibration was based on three major events [28]: Ascomycota crown group (487–773 Mya), Orbiliomycetes–other Pezizomycotina (353–554 Mya), Saccharomycotina crown group (276–514 Mya) and one fossil calibration point (node 9: >100 Mya) [29]. The clock model was set to independent rates, with a burn-in of 20,000, 100,000 samples, a sampling frequency of 10, and the JC69 model. Tracer v.1.7.1 [66] was used to visually check the convergence of parameters across replicate MCMC chains. All resulting effective sample sizes (ESS) ranged from 275 to 1,299 (S4 Table), indicating that the parameters across replicate MCMC chains achieved convergence (with ESS values expected to exceed 200).

RNA-seq data analysis

Raw reads from both WT and Δ*AO414* samples were examined using FastQC. To obtain clean data, fastp (v.4.10.0) [67] was used with default parameters to filter adaptor sequences and remove low-quality reads. The reference genome and gene model annotation files for *A. oligospora* ATCC 24927 were downloaded from NCBI's Genome Browser. Genome indexing was performed using 'hisat2-build' in Hisat2 (v.2.2.1) [68], incorporating splice sites and exon information. The filtered paired-end reads were aligned to the reference genome using Hisat2. Gene abundance for each sample was estimated using featureCounts (v.2.0.3) [69] from the aligned BAM files. Differential expression analysis was conducted using the DESeq2 R package (v.1.30.1) [69]. DESeq2 employs statistical tests to identify differential expression in digital gene expression data based on the negative binomial distribution. Resulting p-values were adjusted using the Benjamini–Hochberg approach to control the false discovery rate.

Temperature and metal ion assays

Conidial suspensions (50 μL) were collected and quantified using a hemocytometer. Subsequently, 100 μL of fungal spore suspensions (800 spores/μL) were added to 6

cm Petri dishes containing water agar (20 g/L agar in 1 L double-distilled water (ddH_2O). Water agar prepared with tap water (Kunming Water Supply Company) was used as a negative control. All fungal dishes were incubated at 12 °C, 20 °C, and 28 °C for 7 days. Trapping devices on each plate were observed and counted under a microscope. For colony growth analysis, fungal strains were cultivated on 9 cm diameter PDA plates at 16 °C, 20 °C, 24 °C, and 28 °C for 6 days, and the diameter of each colony was measured. All experiments were conducted with at least three replicates.

Acknowledgments: We would like to thank the School of Chemical Science and Technology, Key Laboratory of Medicinal Chemistry for Natural Resource - Ministry of Education, Yunnan University for providing us with TEM-EDX. We wish to thank Longchun Bian, for support with the Energy Dispersive X-ray Spectroscopy analyses and data reduction. We would like to thank the Institutional Center for Shared Technologies and Facilities of Kunming Institute of Zoology, Chinese Academy of Sciences, for providing us with transmission electron microscopy. We are grateful to Yingqi Guo for her great help in preparing TEM samples and taking/analyzing TEM images.

Funding

This work was sponsored by Program 202201BF070001-012 of "Double tops" from Yunnan Province and Yunnan University and 2022KF001 from State Key Laboratory for Conservation and Utilization of Bio-Resources in Yunnan. This work was sponsored by National Natural Science Foundation of China 21977086 and 21867018, Yunnan University Program awarded to X.N. (XT412003).

Competing Interests: The authors declare no competing interests.

Data availability

Our sequences files of transcriptome are accessible from the National Center for Biotechnology Information (NCBI) under BioProject accession: PRJNA639935 (https://www.ncbi.nlm.nih.gov/bioproject/PRJNA1073725).

Author Contributions

Conceptualization: Xuemei Niu.

Data curation: Jiao Zhou, Qunfu Wu, Li Wu.

Formal analysis: Jiao Zhou, Qunfu Wu, Li Wu, Junxian Yan.

Investigation: Jiao Zhou, Qunfu Wu, Li Wu, Junxian Yan, Qianyi Cheng, Donglou Wang.

Methodology: Jiao Zhou, Qunfu Wu.

Project administration: Xuemei Niu.

Software: Jiao Zhou, Qunfu Wu.

Supervision: Xuemei Niu.

Validation: Xuemei Niu.

Writing – original draft: Jiao Zhou, Qunfu Wu, Xuemei Niu.

Writing – review & editing: Jiao Zhou, Qunfu Wu, Xuemei Niu.

References:

1. Galy B, Conrad M, Muckenthaler M. Mechanisms controlling cellular and systemic iron homeostasis. Nat Rev Mol Cell Biol. 2024; 25:133-55. https://doi.org/10.1038/s41580-023-00648-1. PMID: 37783783.
2. Li H, Xia X, Tan X, Zang J, Wang Z, Ei-Seedi HR, et al. Advancements of nature nanocage protein: preparation, identification and multiple applications of ferritins. Crit Rev Food Sci Nutr. 2022; 62:7117-28. https://doi.org/10.1080/10408398.2021.1911925. PMID: 33860692.
3. Lampe RH, Coale TH, McQuaid JB, Allen AE. Molecular mechanisms for iron uptake and homeostasis in marine eukaryotic phytoplankton. Annu Rev Microbiol. 2024. https://doi.org/10.1146/annurev-micro-041222-023252. PMID: 39018471.
4. Misslinger M, Hortschansky P, Brakhage AA, Haas H. Fungal iron homeostasis with a focus on *Aspergillus fumigatus*. Biochim Biophys Acta. 2021; 1868(1):118885. https://doi.org/10.1016/j.bbamcr.2020.118885. PMID: 33045305.
5. Arosio P, Elia L, Poli M. Ferritin, cellular iron storage and regulation. IUBMB Life. 2017; 69(6):414-22. https://doi.org/10.1002/iub.1621. PMID: 28349628.
6. Honarmand EK, Bill E, Hagedoorn PL, Hagen WR. The catalytic center of ferritin regulates iron storage via Fe(II)-Fe(III) displacement. Nat Chem Biol. 2012; 8(11):941-8. https://doi.org/10.1038/nchembio.1071. PMID: 23001032.
7. Yi W, Zhang J, Huang Y, Zhan Q, Zou M, Cheng X, et al. Ferritin-mediated mitochondrial iron homeostasis is essential for the survival of hematopoietic stem cells and leukemic stem cells. Leukemia. 2024; 38(5):1003-18. https://doi.org/10.1038/s41375-024-02169-y. PMID: 38402368.
8. Zhou J, Wang D, Wu Q, Jiang Y, Yan J, Wu L, et al. Rare NRPS gene cluster for desferriferrichrome biosynthesis controls the conflict between trap formation and nematicidal activity in *Arthrobotrys oligospora*. J Agric Food Chem. 2024; 72(7):3560-71. https://doi.org/10.1021/acs.jafc.3c08354. PMID: 38340066.
9. Hider RC, Kong X. Chemistry and biology of siderophores. Nat Prod Rep. 2010; 27(5):637-57. https://doi.org/10.1039/B906679A. PMID: 20376388.
10. Yang Y, Yang E, An Z, Liu X. Evolution of nematode-trapping cells of predatory fungi of the Orbiliaceae based on evidence from rRNA-encoding DNA and multiprotein sequences. Proc Natl Acad Sci USA. 2007; 104(20):8379-84. https://doi.org/10.1073/pnas.0702770104. PMID: 17494736.
11. Niu XM, Zhang KQ. *Arthrobotrys oligospora*: a model organism for understanding the interaction between fungi and nematodes. Mycology. 2011; 2(2):59-78. https://doi.org/10.1080/21501203.2011.562559.
12. Yang E, Xu L, Yang Y, Zhang X, Xiang M, Wang C, et al. Origin and evolution of carnivorism in the Ascomycota (fungi). Proc Natl Acad Sci USA. 2012; 109(27):10960-5. https://doi.org/10.1073/pnas.1120915109. PMID: 22715289.
13. Ji X, Yu Z, Yang J, Xu J, Zhang Y, Liu S, et al. Expansion of adhesion genes drives pathogenic adaptation of nematode-trapping fungi. iScience. 2020; 23(5):101057. https://doi.org/10.1016/j.isci.2020.101057. PMID: 32339992.
14. Pokhare SS, Mhatre PH, Manjunatha N, Patil D, Agarrwal R. Fungal biocontrol agents for nematode management in organic agriculture. In: Chaudhary KK, Meghvansi MK, Siddiqui S,

editors. Sustainable Management of Nematodes in Agriculture, Vol2: Role of Microbes-Assisted Strategies. Cham: Springer International Publishing; 2024. p. 183-206.

15. Naranjo-Ortiz MA, Gabaldón T. Fungal evolution: cellular, genomic and metabolic complexity. Biol Rev. 2020; 95(5):1198-232. https://doi.org/10.1111/brv.12605. PMID: 32301582.

16. Porter DL, Naleway SE. Hyphal systems and their effect on the mechanical properties of fungal sporocarps. Acta Biomater. 2022; 145:272-82. https://doi.org/10.1016/j.actbio.2022.04.011. PMID: 35421618.

17. Veenhuis M, Nordbring-Hertz B, Harder W. An electron-microscopical analysis of capture and initial stages of penetration of nematodes by *Arthrobotrys oligospora*. Antonie Van Leeuwenhoek. 1985; 51(4):385-98. https://doi.org/10.1007/BF02275043. PMID: 4091541.

18. Xie M, Bai N, Yang X, Liu Y, Zhang KQ, Yang J. Fus3 regulates asexual development and trap morphogenesis in the nematode-trapping fungus *Arthrobotrys oligospora*. iScience. 2023; 26(8). https://doi.org/10.1016/j.isci.2023.107404. PMID: 37609635.

19. Hodoroaba VD. Chapter 4.4 - Energy-dispersive X-ray spectroscopy (EDS). In: Hodoroaba V-D, Unger WES, Shard AG, editors. Characterization of Nanoparticles: Elsevier; 2020. p. 397-417.

20. Li L, Chen OS, Ward DM, Kaplan J. CCC1 Is a transporter that mediates vacuolar iron storage in yeast. J Biol Chem. 2001; 276(31):29515-9. https://doi.org/10.1074/jbc.M103944200. PMID: 11390404.

21. Gsaller F, Eisendle M, Lechner BE, Schrettl M, Lindner H, Müller D, et al. The interplay between vacuolar and siderophore-mediated iron storage in *Aspergillus fumigatus*. Metallomics. 2012; 4(12):1262-70. https://doi.org/10.1039/c2mt20179h. PMID: 23151814.

22. Lapinskas PJ, Lin SJ, Culotta VC. The role of the Saccharomyces cerevisiae CCC1 gene in the homeostasis of manganese ions. Mol Microbiol. 1996; 21(3):519-28. https://doi.org/10.1111/j.1365-2958.1996.tb02561.x. PMID: 8866476.

23. Briat JF, Lobréaux S. Iron transport and storage in plants. Trends Plant Sci. 1997; 2(5):187-93. https://doi.org/10.1016/S1360-1385(97)85225-9.

24. Briat JF, Duc C, Ravet K, Gaymard F. Ferritins and iron storage in plants. Biochim Biophys Acta Gen Subj. 2010; 1800(8):806-14. https://doi.org/10.1016/j.bbagen.2009.12.003. PMID: 20026187.

25. Segond D, Abi KE, Buisson C, Daou N, Kallassy M, Lereclus D, et al. Iron acquisition in *Bacillus cereus*: The roles of IlsA and Bacillibactin in exogenous ferritin iron mobilization. PLoS Path. 2014; 10(2):e1003935. https://doi.org/10.1371/journal.ppat.1003935. PMID: 24550730.

26. Grant CR, Amor M, Trujillo HA, Krishnapura S, Iavarone AT, Komeili A. Distinct gene clusters drive formation of ferrosome organelles in bacteria. Nature. 2022; 606(7912):160-4. https://doi.org/10.1038/s41586-022-04741-x. PMID: 35585231.

27. Byrne ME, Ball DA, Guerquin-Kern JL, Rouiller I, Wu TD, Downing KH, et al. *Desulfovibrio magneticus* RS-1 contains an iron- and phosphorus-rich organelle distinct from its bullet-shaped magnetosomes. Proc Natl Acad Sci USA. 2010; 107(27):12263-8. https://doi.org/10.1073/pnas.1001290107. PMID: 20566879.

28. Beimforde C, Feldberg K, Nylinder S, Rikkinen J, Tuovila H, Dörfelt H, et al. Estimating the Phanerozoic history of the Ascomycota lineages: Combining fossil and molecular data. Mol

Phylogen Evol. 2014; 78:386-98. https://doi.org/10.1016/j.ympev.2014.04.024. PMID: 24792086.

29. Schmidt AR, Dörfelt H, Perrichot V. *Palaeoanellus dimorphus* gen. et sp. nov. (Deuteromycotina): a Cretaceous predatory fungus. Am J Bot. 2008; 95(10):1328-34. https://doi.org/10.3732/ajb.0800143. PMID: 21632336.

30. Shen XX, Opulente DA, Kominek J, Zhou X, Steenwyk JL, Buh KV, et al. Tempo and mode of genome evolution in the budding yeast subphylum. Cell. 2018; 175(6):1533-45.e20. https://doi.org/10.1016/j.cell.2018.10.023. PMID: 30415838.

31. Whitfield JB. Estimating the age of the polydnavirus/braconid wasp symbiosis. Proc Natl Acad Sci USA. 2002; 99(11):7508-13. https://doi.org/10.1073/pnas.112067199. PMID: 12032313.

32. Langley CH, Fitch WM. An examination of the constancy of the rate of molecular evolution. J Mol Evol. 1974; 3(3):161-77. https://doi.org/10.1007/BF01797451. PMID: 4368400.

33. Chen L, Qiu Q, Jiang Y, Wang K, Lin Z, Li Z, et al. Large-scale ruminant genome sequencing provides insights into their evolution and distinct traits. Science. 2019; 364(6446):eaav6202. https://doi.org/10.1126/science.aav6202. PMID: 31221828.

34. Crowley TJ, North GR. Abrupt climate change and extinction events in Earth history. Science. 1988; 240(4855):996-1002. https://doi.org/10.1126/science.240.4855.996. PMID: 17731712.

35. Mayhew PJ, Bell MA, Benton TG, McGowan AJ. Biodiversity tracks temperature over time. Proc Natl Acad Sci USA. 2012; 109(38):15141-5. https://doi.org/10.1073/pnas.1200844109. PMID: 22949697.

36. Sun Y, Joachimski MM, Wignall PB, Yan C, Chen Y, Jiang H, et al. Lethally hot temperatures during the early Triassic greenhouse. Science. 2012; 338(6105):366-70. https://doi.org/10.1126/science.1224126. PMID: 23087244.

37. Scotese CR, Song H, Mills BJW, van der Meer DG. Phanerozoic paleotemperatures: The earth's changing climate during the last 540 million years. Earth-Sci Rev. 2021; 215:103503. https://doi.org/10.1016/j.earscirev.2021.103503.

38. Kent DV, Muttoni G. Pangea B and the Late Paleozoic Ice Age. Palaeogeogr Palaeoclimatol Palaeoecol. 2020; 553:109753. https://doi.org/10.1016/j.palaeo.2020.109753.

39. Montañez IP, Poulsen CJ. The late Paleozoic ice age: An evolving paradigm. Annu Rev Earth Planet Sci. 2013; 41(1):629-56. https://doi.org/10.1146/annurev.earth.031208.100118.

40. Yang X, Chen Y, Zhang L, He J, Wu Q, Li S, et al. Melanin precursors mediated adaption to temperature changes in fungus and animal via inhibition of lipid-mediated ferroptosis. Sci China Life Sci. 2023; 66(8):1800-17. https://doi.org/10.1007/s11427-022-2265-6. PMID: 36949229.

41. Corradini E, Buzzetti E, Pietrangelo A. Genetic iron overload disorders. Mol Aspects Med. 2020; 75:100896. https://doi.org/10.1016/j.mam.2020.100896. PMID: 32912773.

42. Camaschella C. Understanding iron homeostasis through genetic analysis of hemochromatosis and related disorders. Blood. 2005; 106(12):3710-7. https://doi.org/10.1182/blood-2005-05-1857. PMID: 16030190.

43. Adams PC, Reboussin DM, Barton JC, McLaren CE, Eckfeldt JH, McLaren GD, et al. Hemochromatosis and iron-overload screening in a racially diverse population. New Engl J Med. 2005; 352(17):1769-78. https://doi.org/10.1056/NEJMoa041534. PMID: 15858186.

44. Motulsky AG, Beutler E. Population screening in hereditary hemochromatosis. Annu Rev

Public Health. 2000; 21(Volume 21, 2000):65-79. https://doi.org/10.1146/annurev.publhealth.21.1.65. PMID: 10884946.

45. Gerwien F, Skrahina V, Kasper L, Hube B, Brunke S. Metals in fungal virulence. FEMS Microbiol Rev. 2018; 42(1):fux050. https://doi.org/10.1093/femsre/fux050. PMID: 29069482.

46. Sorribes-Dauden R, Peris D, Martínez-Pastor MT, Puig S. Structure and function of the vacuolar Ccc1/VIT1 family of iron transporters and its regulation in fungi. Comput Struct Biotechnol J. 2020; 18:3712-22. https://doi.org/10.1016/j.csbj.2020.10.044. PMID: 33304466.

47. Pijuan J, Moreno DF, Yahya G, Moisa M, Ul Haq I, Krukiewicz K, et al. Regulatory and pathogenic mechanisms in response to iron deficiency and excess in fungi. Microb Biotechnol. 2023; 16(11):2053-71. https://doi.org/10.1111/1751-7915.14346. PMID: 37804207.

48. Blatzer M, Latgé JP. Metal-homeostasis in the pathobiology of the opportunistic human fungal pathogen *Aspergillus fumigatus*. Curr Opin Microbiol. 2017; 40:152-9. https://doi.org/10.1016/j.mib.2017.11.015. PMID: 29179120.

49. Sur S, Sharma A. Understanding the role of temperature in seasonal timing: Effects on behavioural, physiological and molecular phenotypes. Mol Ecol. 2024; 00(n/a):e17447. https://doi.org/10.1111/mec.17447. PMID: 38946196.

50. Ma CS, Ma G, Pincebourde S. Survive a warming climate: Insect responses to extreme high temperatures. Annu Rev Entomol. 2021; 66(Volume 66, 2021):163-84. https://doi.org/10.1146/annurev-ento-041520-074454. PMID: 32870704.

51. Knapp BD, Huang KC. The effects of temperature on cellular physiology. Annu Rev Biophys. 2022; 51(Volume 51, 2022):499-526. https://doi.org/10.1146/annurev-biophys-112221-074832. PMID: 35534014.

52. Dohnalová H, Matoušková E, Lankaš F. Temperature-dependent elasticity of DNA, RNA, and hybrid double helices. Biophys J. 2024; 123(5):572-83. https://doi.org/10.1016/j.bpj.2024.01.032. PMID: 38340722.

53. Trip DSL, Youk H. Yeasts collectively extend the limits of habitable temperatures by secreting glutathione. Nat Microbiol. 2020; 5(7):943-54. https://doi.org/10.1038/s41564-020-0704-2. PMID: 32313201.

54. Nagasaka S, Nishizawa NK, Watanabe T, Mori S, Yoshimura E. Evidence that electron-dense bodies in *Cyanidium caldarium* have an iron-storage role. BioMetals. 2003; 16(3):465-70. https://doi.org/10.1023/A:1022563600525. PMID: 12680710.

55. Su H, Zhao Y, Zhou J, Feng H, Jiang D, Zhang KQ, et al. Trapping devices of nematode-trapping fungi: formation, evolution, and genomic perspectives. Biol Rev. 2017; 92(1):357-68. https://doi.org/10.1111/brv.12233. PMID: 26526919.

56. He ZQ, Wang LJ, Wang YJ, Chen YH, Wen Y, Zhang KQ, et al. Polyketide synthase–terpenoid synthase hybrid pathway regulation of trap formation through ammonia metabolism controls soil colonization of predominant nematode-trapping fungus. J Agric Food Chem. 2021; 69(15):4464-79. https://doi.org/10.1021/acs.jafc.1c00771. PMID: 33823587.

57. Sheraz S, Wan Y, Venter E, Verma SK, Xiong Q, Waites J, et al. Subcellular dynamics studies of iron reveal how tissue-specific distribution patterns are established in developing wheat

grains. New Phytol. 2021; 231(4):1644-57. https://doi.org/10.1111/nph.17440. PMID: 33914919.

58. Pertea G, Pertea M. GFF utilities: GffRead and GffCompare [version 1; peer review: 3 approved]. F1000Research. 2020; 9(304). https://doi.org/10.12688/f1000research.23297.1.

59. Simão FA, Waterhouse RM, Ioannidis P, Kriventseva EV, Zdobnov EM. BUSCO: assessing genome assembly and annotation completeness with single-copy orthologs. Bioinform. 2015; 31(19):3210-2. https://doi.org/10.1093/bioinformatics/btv351. PMID: 26059717.

60. Blin K, Shaw S, Augustijn HE, Reitz ZL, Biermann F, Alanjary M, et al. antiSMASH 7.0: new and improved predictions for detection, regulation, chemical structures and visualisation. Nucleic Acids Res. 2023; 51(W1):W46-W50. https://doi.org/10.1093/nar/gkad344. PMID: 37140036.

61. Gilchrist CLM, Booth TJ, van Wersch B, van Grieken L, Medema MH, Chooi YH. cblaster: a remote search tool for rapid identification and visualization of homologous gene clusters. Bioinform adv. 2021; 1(1):vbab016. https://doi.org/10.1093/bioadv/vbab016. PMID: 36700093.

62. Emms DM, Kelly S. OrthoFinder: phylogenetic orthology inference for comparative genomics. Genome Biol. 2019; 20(1):238. https://doi.org/10.1186/s13059-019-1832-y. PMID: 31727128.

63. Edgar RC. Search and clustering orders of magnitude faster than BLAST. Bioinform. 2010; 26(19):2460-1. https://doi.org/10.1093/bioinformatics/btq461. PMID: 20709691.

64. Törönen P, Medlar A, Holm L. PANNZER2: a rapid functional annotation web server. Nucleic Acids Res. 2018; 46(W1):W84-W8. https://doi.org/10.1093/nar/gky350. PMID: 29741643.

65. Minh BQ, Schmidt HA, Chernomor O, Schrempf D, Woodhams MD, von Haeseler A, et al. IQ-TREE 2: New models and efficient methods for phylogenetic inference in the genomic era. Mol Biol Evol. 2020; 37(5):1530-4. https://doi.org/10.1093/molbev/msaa015. PMID: 32011700.

66. Rambaut A, Drummond AJ, Xie D, Baele G, Suchard MA. Posterior summarization in Bayesian phylogenetics using Tracer 1.7. Syst Biol. 2018; 67(5):901-4. https://doi.org/10.1093/sysbio/syy032. PMID: 29718447.

67. Chen S, Zhou Y, Chen Y, Gu J. fastp: an ultra-fast all-in-one FASTQ preprocessor. Bioinform. 2018; 34(17):i884-i90. https://doi.org/10.1093/bioinformatics/bty560. PMID: 30423086.

68. Kim D, Paggi JM, Park C, Bennett C, Salzberg SL. Graph-based genome alignment and genotyping with HISAT2 and HISAT-genotype. Nat Biotechnol. 2019; 37(8):907-15. https://doi.org/10.1038/s41587-019-0201-4. PMID: 31375807.

69. Liao Y, Smyth GK, Shi W. featureCounts: an efficient general purpose program for assigning sequence reads to genomic features. Bioinform. 2014; 30(7):923-30. https://doi.org/10.1093/bioinformatics/btt656. PMID: 24227677.

1054 **Supporting information**

1055 **S1 Table**. **The primers were used in this study**

1056 **S2 Table. Gain and loss of iron-related genes in NTFs**

1057 **S3 Table. Distribution patterns of *Ao414* gene cluster across 1,488 high-quality**

1058 **fungal genomes**

1059 **S4 Table**. **Results of Tracer based on report of the MCMC runs**

1060 **S1 Fig. Construction and PCR and Southern blot analysis of two mutants**

1061 **Δ*Ao414* and Δ*Ao415*.**

1062 **S2-1 Fig. Evaluation of the functions of desferriferrichrome in iron distribution**

1063 **and storage in *A. oligospora* mycelia.** (**a-d**)**,** Energy Dispersive X-ray Spectroscopy

1064 (EDX) analysis of WT mycelia treated with only solvent DMSO. EDX profiles from

1065 ferrichrome (**a**), autophagosomes (**b**), mitochondria (**c**), and cell walls (**d**) respectively,

1066 normalized for the Cu content from the TEM support grid. The peak at ~0.1 KeV,

1067 partially outside the y-axis scale, is carbon. **e,** Semi-quantitative analysis of EDX

1068 profiles. All values are percentage atomic weight, and the average of 3 areas for same

1069 organelle. Values for Fe are marked in orange (**e**).

1070 **S2-2 Fig. Evaluation of the functions of desferriferrichrome in iron distribution**

1071 **and storage in *A. oligospora* mycelia.** (**a–d**)**,** Energy Dispersive X-ray Spectroscopy

1072 (EDX) analysis of WT mycelia treated with desferriferrichrome. EDX profile from

1073 ferrichrome (**a**), autophagosomes (**b**), mitochondria (**c**), and cell walls (**d**),

1074 respectively, normalized for the Cu content from the TEM support grid. The peak at

1075 ~0.1 KeV, partially outside the y-axis scale, is carbon. **e**, Semi-quantitative analysis of

1076 EDX profiles. All values are percentage atomic weight, and the average of 3 areas for
1077 same organelle. Values for Fe are marked in orange (**e**).

1078 **S2-3 Fig. Evaluation of the functions of desferriferrichrome in iron distribution**
1079 **and storage in *A. oligospora* mycelia.** (**a–d**)**,** Energy Dispersive X-ray Spectroscopy
1080 (EDX) analysis of *Δ414* mycelia treated with only solvent DMSO. EDX profiles from
1081 ferrichrome (**a**), autophagosomes (**b**), mitochondria (**c**), cell walls (**d**), respectively,
1082 normalized for the Cu content from the TEM support grid. The peak at ~0.1 KeV,
1083 partially outside the y-axis scale, is carbon. **e**, Semi-quantitative analysis of EDX
1084 profiles. All values are percentage atomic weight, and the average of 3 areas for same
1085 organelle. Values for Fe are marked in orange (**e**).

1086 **S2-4 Fig. Evaluation of the functions of desferriferrichrome in iron distribution**
1087 **and storage in *A. oligospora* mycelia.** (**a–d**), Energy Dispersive X-ray Spectroscopy
1088 (EDX) analysis of the *Δ414*+ mycelia treated with desferriferrichrome. EDX profiles
1089 from ferrichrome (**a**), autophagosomes (**b**), mitochondria (**c**), and cell walls (**d**),
1090 respectively, normalized for the Cu content from the TEM support grid. The peak at
1091 ~0.1 KeV, partially outside the y-axis scale, is carbon. **e**, Semi-quantitative analysis of
1092 EDX profiles. All values are percentage atomic weight, and the average of 3 areas for
1093 same organelle. Values for Fe are marked in orange (**e**).

1094 **S3 Fig. Evaluation of desferriferrichrome functions in the organelles and iron**
1095 **distribution in the trapping devices of *A. oligospora*.** (**a**–**d**), Energy Dispersive
1096 X-ray Spectroscopy (EDX) analysis of the trapping devices of WT treated with only
1097 solvent DMSO. EDX profiles from electron dense body (**a**), mitochondria (**b**),

1098 vacuole (**c**), and cell walls (**d**), respectively, normalized for the Cu content from the
1099 TEM support grid. The peak at ~0.1 KeV, partially outside the y-axis scale, is carbon.
1100 **e**, Semi-quantitative analysis of EDX profiles. All values are percentage atomic
1101 weight, and the average of 3 areas for same organelle. Values for Fe are marked in
1102 orange (**e**).

1103 **S4 Fig. Evaluation of desferriferrichrome functions in the organelles and iron**
1104 **distribution in the trapping devices of *A. oligospora*.** (**a–e**), Energy Dispersive
1105 X-ray Spectroscopy (EDX) analysis of in the trapping devices of WT treated with 30
1106 μM Fe^{3+}solution. EDX profiles from ferrichrome (**a**), electron dense body (**b**),
1107 mitochondria (**c**), cytoplasm (**d**), and cell walls (**e**), respectively, normalized for the
1108 Cu content from the TEM support grid. The peak at ~0.1 KeV, partially outside the
1109 y-axis scale, is carbon. **f**, Semi-quantitative analysis of EDX profiles. All values are
1110 percentage atomic weight, and the average of 3 areas for same organelle. Values for
1111 Fe are marked in orange (**f**).

1112 **S5 Fig. Maximum likelihood tree of nematode-trapping fungi.**
1113 (**a**), Tree inferred with concatenated 1136 sets of 1:1 orthologous protein coding genes.
1114 (**b**), the 1st-2nd codon nucleotide of orthologous genes. (**c**), the 3nd codon nucleotide
1115 of orthologous genes. (**d**), ASTRAL tree based on 1136 orthologous gene tree.
1116 Maximum likelihood phylogenetic tree were constructed by IQ-TREE2. 1000
1117 replicates of bootstraps are conducted to compute the node support. Bootstrap values
1118 were marked at each node.

1119 **S6 Fig. DensiTree showing incongruence among gene trees.** A total of 1136 gene
1120 trees were drawn using IQtree. The consensus tree is shown by the bold black line.

1121 Topology of each gene tree is shown by the transparent green lines.

1122 **S7 Fig. Expression levels change of Ferritin gene in Δ*Ao414* vs. WT. Gene**

1123 **expression level was measured by RNA-seq.** Statistical methods:

1124 Wald significance tests.

1125 **S8 Fig. Loss of five key iron-related genes during Late Paleozoic Ice Age.**